Carbon erosion and deposition on the divertor of W7-X during the operational period OP1.2b

M. Mayer[a], M. Balden[a], S. Brezinsek[c], V.V. Burwitz[a], C. Cupak[f], C.P. Dhard[b], S. Elgeti[a], M. Guitart Corominas[a], P. Hiret[a], M. Kandler[a], D. Naujoks[b], J.-H. Schmidt-Dencker[a], C. Ruset[d], T.B. Saramela[e], T.F. Silva[e], and W7-X Team

[a] *Max-Planck-Institut für Plasmaphysik, Garching, Germany*
[b] *Max-Planck-Institut für Plasmaphysik, Greifswald, Germany*
[c] *Forschungszentrum Jülich GmbH, Jülich, Germany*
[d] *National Institute for Laser, Plasma and Radiation Physics, Bucharest, Romania*
[e] *University of São Paulo, São Paulo, Brazil*
[f] *Institute of Applied Physics, TU Wien, Vienna, Austria*

Abstract

The net erosion and deposition pattern of carbon from the Test Divertor Unit (TDU) of the stellarator W7-X was determined during the operational phase OP1.2b in the year 2018. In total 18 special target elements with marker layers consisting of about 300 nm molybdenum and 5-10 µm carbon on top were used in all 10 TDUs. The thicknesses of the marker layers were determined by elastic backscattering spectrometry (EBS) using 2.5 MeV protons before and after plasma exposure; scanning electron microscopy (SEM) was used for investigating the surface morphology before and after exposure. Plasma-exposed surfaces were considerably smoother than unexposed surfaces with decreased mean roughness and a shift of the inclination angle distribution towards lower values. The erosion on the 10 TDUs was unequal within a factor of about two. In total 20.4±5.7 g carbon were eroded from the 10 TDUs. Some deposition of carbon is observed on the TDUs adjacent to the strike line. Compared to the operational period OP1.2a in 2017 the net carbon erosion rate dropped by a factor of 5-6 due to regular boronizations, which reduced the oxygen (and subsequently also the carbon) content in the plasma by 1-2 orders of magnitude.

1. Introduction

The Wendelstein 7-X (W7-X) experiment [1,2,3,4] is an advanced stellarator with superconducting coils and a plasma volume of 30 m^3. Plasma operation started in 2015. Since the second operational phase (OP 1.2) in the years 2017 and 2018 an adiabatically cooled divertor, the so-called Test Divertor Unit (TDU) [5,6], was used. This divertor was complemented by baffles, the inner wall was covered by the inner heat shield. Most PFCs (except of the outer wall and pumping gap panels) were made of fine-grain graphite. The W7-X divertor implements the island divertor concept [7] with chains of magnetic islands at the plasma edge providing multiple x-points. The plasma therefore intersects the divertor plates at some distance from the closed flux surfaces. This concept was initially developed at the antecessor experiment W7-AS [8]. The TDU had the same plasma-facing shape as the water-cooled steady-state

divertor with carbon-fiber-composite PFCs that has been installed in the years 2019 – 2021 and will be in operation starting in the year 2022. This divertor should finally allow long-pulse discharges up to 1800 s.

The investigation of plasma-wall interactions (PWI) in W7-X is challenging due to the three-dimensional plasma geometry and the bent shape of all PFCs, the high heat loads at the divertor strike lines of up to 10 MW/m^2 and the large sizes of most PFCs. Despite these difficulties OP 1.2 offered the unique possibility to study PWI phenomena in W7-X in some detail using surface-analytical techniques due to the adiabatic cooling. This will be no longer possible in OP 2 and beyond, where the requirement for water-cooled plasma-exposed surfaces severely limits the possibilities for sample exposure and exchange. For PWI investigations 18 exchangeable divertor target elements were coated with C/Mo marker layers. One set of elements was exposed during the operational phase OP 1.2a in 2017 [9] and exchanged during the vessel opening between the operational phases OP 1.2a and OP 1.2b. The erosion/deposition pattern observed after OP 1.2a was already described in [9]. This paper describes the results observed in OP 1.2b.

In OP 1.2a, wall conditioning was performed using glow discharge cleaning (GDC) only and without boronizations. In OP 1.2b, three boronizations were applied. This resulted in a substantial decrease of the oxygen and carbon concentrations in the plasma [10,11]: After the third boronization the oxygen levels were about two orders of magnitude lower compared to the pre-boronization values, while Z_{eff} decreased from 4.5 to values close to 1.2 in reference discharges. This decrease of the low-Z impurity concentration significantly extended the operational window of W7-X towards higher plasma densities (the line-integrated electron density increased from 4×10^{19} m^{-2} to more than 1×10^{20} m^{-2}) and the diamagnetic energy increased from 330 kJ to 510 kJ [10,12]. This decrease was also associated with a substantial change of the erosion/deposition behavior on the TDU, which is described in this paper.

2. Experimental

2.1 Plasma operation and wall conditioning

The operational phase OP 1.2a lasted from August to December 2017 and consisted of 1248 plasma discharges with a total plasma time of 3776 s, see Table 1. For details of different plasma configurations see [9, Table 1 or 13, Table 1]. Most discharges with 65.7% of the plasma time were in Standard configuration, the remaining discharges were in High Iota or High Mirror configuration while Low Iota discharges were not performed. 72.2% of the plasma time were nominally He fueled discharges, however, even in the case of He fueling the plasmas were usually mixed H+He discharges with varying and often only small He content.

The operational phase OP 1.2b lasted from July to October 2018 and had a total plasma duration of 9054 s, see Table 1 or [13, Table 2]. Most discharges (4809 s, 53.1% of the plasma time) were in Standard configuration, the remaining discharges were in Low Iota (1180 s), High Iota (1673 s) or High Mirror (1392 s) configuration. All configurations have their strike lines on different areas of the TDU [6]. All discharges were in hydrogen, deuterium discharges were not performed in OP 1.2a or 1.2b. While various types of divertor plasmas were performed, more exotic configurations were limited in time. The

dominant plasma scenario in OP 1.2b had a pulse duration of about 10 s, medium ECR heating power of 3 to 4 MW, and attached divertor conditions.

The Standard Configuration has its strike line on the horizontal target modules TM1h to TM4h and the vertical target modules TM1v to TM3v, see Fig. 1 for a schematic representation of the modules, the High Mirror configuration has the strike line on TM1v to TM3v and TM3h to TM4h. The High Iota configuration has the strike line in the high iota part of the divertor outside of the investigated area of this study. See e.g. [6] for details of the different plasma configurations. Peak divertor heat loads of up to 8 MW/m^2 and strike line widths of up to 11 cm were observed using infrared thermography. The plasma wetted divertor area increased about linearly with ECRH heating power up to values of 1.5 m^2 at 5 MW [6]. The divertor bulk target temperature increased throughout the experimental day, seldomly up to 400 °C [6]. The surface temperature at the strike line could reach temperatures up to 800 °C [14]. The electron temperature in the scrape-off layer was 50 – 100 eV with electron densities of 2 – 6×10^{18} m^{-3} [15, 16].

While no boronizations were applied in OP 1.2a, three boronizations were applied in OP 1.2b. As result of the boronizations, thin boron layers (typically containing also carbon and oxygen) with thicknesses of a few 10 nm were found on all wall elements in W7-X [17].

2.2 Exchangeable PWI target elements in the TDU

Special exchangeable PWI target elements for erosion/deposition investigations were developed [18], a schematic representation can be found in [9, Fig. 1]. W7-X has 10 TDUs of which 5 are lower TDUs (1l to 5l) and 5 upper TDUs (1u to 5u), see e.g. [5, 14] for a schematic representation. In total 18 PWI target elements were used, see Fig. 1 for a schematic representation of the locations of the elements and [9, Table 2] for tabulated positions. The position TM2h6 in the horizontal target was used in all TDUs for studying the toroidal asymmetry of the erosion/deposition pattern, additionally the positions TM1h3 and TM3h6 in the horizontal and TM1v5 and TM2v2 in the vertical targets were used in TDUs 5l and 5u.

2.3 Marker layers for erosion/deposition measurements

Erosion of carbon and deposition of wall materials and impurities, such as C, O, Ni, Fe etc. on the TDU, were determined by using marker layers of 5-10 µm thick carbon layers on top of 200-300 nm molybdenum, which were deposited on the fine grain graphite tiles of the PWI target elements. The Mo interlayer distinguishes the C marker layer from the bulk C of the tile for depth-profiling methods. Both layers were deposited using the CMSII technique [19], see Fig. 2 for an SEM image of the fracture surface of the coatings before plasma exposure.

The marker layers were analyzed before and after exposure in W7-X using Elastic Backscattering Spectrometry (EBS) at the IPP tandem accelerator facility [20]. 2.5 MeV incident protons at normal incidence and a scattering angle of 165° were used, see Figs. 1 and 2 in [21] for typical spectra. A passivated implanted planar silicon (PIPS) detector with a nominal energy resolution of about 12 keV and a thickness of 300 µm was used. In order to monitor the (typically slow) variations of the initial layer thicknesses pre-exposure measurements were performed using a step width of 20 mm. The post-

exposure measurements were then made with a smaller step width of 5 mm. In total almost 3000 spectra were recorded.

The measured spectra were analyzed using the SIMNRA software [22,23] with SRIM [24] stopping powers and non-Rutherford SigmaCalc scattering cross-sections for ^{12}C, ^{13}C and ^{16}O [25]. Surface roughness was taken into account using the simplified model from [26].

The large number of acquired spectra required a special approach. The spectra were fitted using different methods:

1. The measurements before exposure (about 500 spectra) were fitted using automated fits.
2. Two different Artificial Neural Networks (ANNs) were trained [27]. The model ANN 2 consisted of a carbon substrate and two layers: A Mo interlayer and a top carbon layer. Both layers could include roughness. Model ANN 3 had three layers: The Mo interlayer, the top carbon layer, and a mixed carbon/oxygen layer on top. The Mo interlayer and the carbon layer could include roughness.

Once trained the ANNs evaluated a given spectrum in less than 1 s.

Scanning electron microscopy was performed with a FEI Helios nanolab 600 with focused ion beam (FIB) for cross-sectioning and energy dispersive X-ray spectroscopy (EDX) capabilities. The electron beam energy was 5 keV.

Surface roughness measurements were made with the optical 3-dimensional profiler Olympus LEXT 3D Measurement Laser Microscope OLS4000.

3. Results

3.1 Scanning electron microscopy

Photos of the marker tiles at position TM2h6, see Fig. 1, in TDU 2u after the operational period OP 1.2b are shown in Fig. 3 top. Scanning electron micrographs of the surfaces at positions A – H are shown in Fig. 3 bottom, focused ion beam (FIB) cross-sections from positions A – H are shown in Fig. 4. All micrographs were recorded with secondary electrons. The surfaces on tiles 024, E004 and partly on A004 showed only minor modifications by the plasma and the SEM image from position H can be taken as typical representation of the original structure of the marker layers. The initial surfaces are rough on a coarser scale due to the grinding process of the tiles, which results in linear grooves, and show larger hemispherical structures due to the coating process. The fine-grain graphite substrate material shows larger pores. The Mo interlayer with a thickness of 200-300 nm follows the morphology of the substrate and is consequently quite rough, and also the carbon marker layer follows approximately the substrate structure.

Pos. A in Figs. 3 and 4 is an area with low erosion. The hilltop has been somewhat eroded, while the whole surface exhibits a small-scale roughening. Pos. B and C are areas of high erosion. Here the carbon

marker layer has been fully eroded at hilltops and at plasma-inclined surfaces and the Mo interlayer is at the surface, see the red marked areas. In valleys and on plasma-averted hill sides the carbon layer is still present, but is partly eroded. The surface shows a small-scale roughening. However, despite this erosion-initiated small-scale roughness the overall roughness of these erosion-dominated areas is smaller than the roughness of the initial surfaces: The grinding grooves and hills have (more or less) disappeared as well as the initial hemispherical structures (see Pos. H for comparison). Pos. D is between the erosion-dominated areas B and C and the net deposition area on tile 21. Here the valleys exhibit a smoother impression and probably contain thin deposits, while hilltops and plasma-inclined faces show the typical microstructure of erosion areas. Positions E to G show thin deposits with thicknesses below 500 nm, see also Fig. 5. Deposits have a visually smoother appearance than erosion-dominated areas. At the hilltops some small erosion might have occurred, but this is difficult to judge due to the thickness inhomogeneities of the initial layers. Tiles 024 and E004 show only minor modifications by the plasma, see above. Indications for delamination, either of the C marker layer or of the Mo layer, could not be found at any place.

3.2 Surface roughness

The surface morphology was recorded with an optical profiler at position J, see Fig. 3 top, where only minor modifications of the initial surface were observed, and at the high erosion position C using a lateral step width of 0.625 µm in toroidal and poloidal directions. The height profiles consisted of 2-dimensional height maps with about 4700x4700 pixels, covering areas of approximately 3x3 mm^2.

The surface roughness was characterized by the arithmetic mean roughness (sometimes called arithmetic mean deviation) S_A on 4 areas of 232x232 μm^2 each. These smaller areas allowed a more precise fit of the base profile using planes, the S_A values of the 4 different areas were averaged. The S_A value at position J was 2.18 µm, and 0.95 µm at position C. This decrease of the arithmetic mean roughness demonstrates the smoothing effect of the plasma exposure, as can be seen already qualitatively by comparing the visual impression of positions C and H in Figs. 3 and 4.

The arithmetic mean roughness provides only a crude characterization of the roughness. Therefore the local inclination angles φ_i of linear line profiles were determined from

$$\varphi_i = \arctan\left(\frac{z_{i+1}-z_i}{x_{i+1}-x_i}\right),$$

with z_i *and* z_{i+1} being the heights at positions *i* and *i+1*, respectively, and x_i, x_{i+1} being the lateral coordinates at positions *i* and *i+1*. Due to the surface structures (linear grooves and hills) introduced by the grinding process the distributions of inclination angles were determined in poloidal and toroidal directions separately. The grinding direction was parallel to the poloidal direction.

The frequency distributions of the local inclination angles φ_i at positions J and C, see Fig. 3 top, are shown in Fig. 6. The distributions at position J are relatively broad, thus reflecting the relatively large roughness of the initial marker surface, see position H in Figs. 3 and 4. The direction parallel to the grinding is marked by a slightly narrower inclination angle distribution than for the direction perpendicular to the grinding grooves. The high-erosion position C is characterized by considerably

narrower distributions both in poloidal and toroidal directions: This demonstrates the polishing effect of plasma erosion/deposition. The grinding direction still has a slightly narrower distribution than the direction perpendicular to the grinding grooves, but this difference is considerably smaller than at position J. This is a quantitative measure of the visual impression at position C in Figs. 3 and 4, that the grinding grooves are less pronounced after plasma exposure in high-erosion areas.

As described in [28] the 2-dimensional surface profiles were also subdivided in triangles formed by the regular mesh of measured data points and the inclination angles ϕ_i of their (local) surface normals towards the nominal surface normal were determined. The frequency distributions from positions J and C are shown in Fig. 7. The initial distribution at J is relatively wide with a broad maximum at an inclination angle around 26°. The distribution at the high erosion position C is considerably narrower with a maximum at about 15°. The mean inclination angle at position J is 38.4° compared to 23.9° at the high erosion position C. Again, this demonstrates the polishing effect of plasma erosion/deposition, resulting in smoother surfaces with smaller inclination angles after plasma exposure. It should be noted that inclination angle distributions from line profiles, as shown in Fig. 6, and inclination angle distributions from triangular planes, as shown in Fig. 7, are just different views, i.e., 1-dimensional versus 2-dimensional, onto the same roughness.

It has been already shown experimentally and by computer simulations, that the physical sputtering yield of a rough surface can deviate significantly from a smooth surface [29,30,31,32]: At normal incidence the sputtering yield of a (moderately) rough surface is typically higher than that of a smooth surface, while at grazing angles of incidence the physical sputtering yield of a rough surface is lower than that of a smooth surface. It has been already pointed out in [28] that “the governing parameter for description of the sputtering behaviour is the mean value of the surface inclination angle distribution, rather than the commonly used root mean square roughness.” In a fusion device with a magnetically confined plasma, ions typically hit material surfaces at grazing angles of incidence of around 60° [33]. The observed plasma polishing effect of initially rough surfaces by erosion/deposition processes and the observed narrowing of the distribution of inclination angles therefore changes the erosion/deposition balance of the surfaces with incident plasma fluence. A decrease of the surface roughness typically results in an increased physical sputtering yield, especially for incident heavier ions such as boron, carbon or oxygen. The observed plasma smoothing effect with increasing fluence is therefore expected to increase the erosion yield at the plasma strike line with increasing exposure time.

3.3 Erosion/deposition pattern

3.3.1. Horizontal target modules

The initial thicknesses of the Mo and C layers, as determined by EBS on target element TM2h6 in TDU 5l, are shown in Fig. 8 as hollow symbols together with a schematic representation of the target element. The origin of the coordinate system along the target element is the small tip in the middle of the element

in toroidal direction towards the pumping gap, see the red x in Fig. 3 top[1]. The results of the pre-analysis from the two different ANN analyses and the automated fits agree very well. The initial thicknesses of the Mo and C layers on the different tiles show some variations due to the position of the individual tiles in the coating device during the coating process and the application of different coating runs. Some tiles also showed a layer thickness gradient over the length of the tile, the maximum difference on individual tiles was of the order of 10%. This variation of layer thicknesses on different tiles demonstrates the necessity of careful pre-analysis of each individual tile.

The thicknesses of the Mo and C layers, as determined by the ANN 3 analysis of the EBS spectra, are shown in Fig. 8 as solid symbols. From about 100 mm to 220 mm the carbon marker layer thickness after exposure is thinner than before exposure, i.e., in this region the carbon layer has been partly eroded. At the position with maximum erosion around 150 mm, about 10^{19} C-atoms/cm^2 (about 1 µm) still remain, while the Mo layer below has the same thickness as initially. Between 220 and 280 mm the amount of carbon is higher than initially, i.e., this is a net deposition area. At around 350 mm another small net erosion area can be observed.

Deposits consist mostly of carbon, but usually also contain some boron. While the boron signal can sometimes be qualitatively identified, a quantification is difficult due to the overlap of the B and C signals in the EBS spectra. As was shown in [10] the boron content in deposited layers is typically below 5 at.%. The term “carbon” in this paper therefore refers to a carbon-rich mixture of boron and carbon. Oxygen is typically also visible at levels of a few at.%. Due to the porosity of deposited layer [10] it is generally difficult to distinguish if oxygen was incorporated into the layers during plasma operation or during air exposure. Oxygen therefore will be not discussed here. As was already shown using Laser-induced Breakdown Spectroscopy (LIBS), deposited layers typically also contain hydrogen [34,35,36]. This was not visible for the applied analysis methods.

The difference between the layer thicknesses before and after exposure, i.e., the net erosion of C and Mo, is shown in Fig. 9 for target element 5l TM2h6, based on the initial layer thicknesses as shown in Fig. 8. The layer thicknesses before exposure were linearly interpolated between the data points and extrapolated at the tile edges, if necessary. The highest erosion of about $5\text{x}10^{19}$ C-atoms/cm^2 is observed at the strike line at around 150 mm, while a second net erosion area with a maximum erosion of about $1\text{x}10^{19}$ C-atoms/cm^2 is observed at around 350 mm. Net carbon deposition areas are observed at both sides of the strike line area at about 80 mm and 250 mm. The area towards the baffle >400 mm shows almost no changes. The thickness of the Mo-layer below the carbon layer is identical to its initial thickness, i.e., it has been not eroded and there were also no larger scale delaminations.

For some target elements the erosion of the carbon marker layer was small enough such that some carbon of the layer was still present and the underlying Mo interlayer has not been eroded (like in Figs. 8 and 9). However, on some other target elements either the erosion was higher or the initial carbon layer thickness was thinner, so that the carbon marker was fully eroded at the strike line position and the underlying Mo layer was partly eroded. A typical example is shown in Fig. 10. In these cases, only a lower

[1] Ref. [9] used the gap between the first and the second tile as origin of the coordinate system. For target element TM2h6 this is shifted by 64.7 mm compared to the present work and has a different prefix.

value for the net carbon erosion can be directly extracted from the measurements. However, a more realistic value can be obtained by assuming that the invisible carbon erosion (i.e., the carbon erosion exceeding the erosion of the marker layer) is proportional to the Mo erosion. The proportionality factor was determined in areas where both carbon and molybdenum erosion occurred, which is possible due to the laterally inhomogeneous erosion on the microscale. This extrapolation of the net carbon erosion based on the Mo erosion is shown in Fig. 10 as dash-dotted line. Because carbon and molybdenum erosion can have different origins (carbon is potentially eroded by physical sputtering and by chemical erosion, while Mo is eroded only by physical sputtering by heavier plasma impurities) this extrapolation has large uncertainties. This is taken into account by assuming an uncertainty of 33% for the extrapolation: This range of uncertainties is shown as light grey area in Fig. 10.

The erosion pattern on target element TM2h6 in TDU 2u (Fig. 10) is qualitatively very similar to TDU 5l shown in Figs. 8 and 9: High carbon erosion is observed at the strike line from about 80 – 200 mm. On the right-hand side at about 250 mm adjacent to the strike line some deposition of carbon is observed. A second strike line with erosion is observed from about 370 – 420 mm.

The described erosion/deposition pattern is observed on all 10 TDUs on target element TM2h6: High carbon erosion is observed at the strike line from about 80 – 200 mm. On the left-hand side at about 70 mm adjacent to the strike line on some TDUs and on the right-hand side at about 250 mm adjacent to the strike line on all TDUs some deposition of carbon is observed. A second strike line with erosion is observed from about 320 – 370 mm. As can be seen in SEM images the remaining area of the target elements shows thin deposits with thicknesses below the detection limit of EBS, i.e., the thickness of these deposits is below 500 nm. Hilltops in these areas may be somewhat eroded at some places.

The maximum carbon erosion at the strike line position on target element TM2h6 was 9.2-9.3×10^{19} C-atoms/cm^2 (about 10.0-10.2 µm). This was observed in TDUs 2l and 2u and converts to a maximum erosion rate of 1.9×10^{16} C-atoms/(cm^2s) (about 2.1 nm/s). The lowest carbon erosion at the strike line position on target element TM2h6 was observed in TDU 5l and was 4.5×10^{19} C-atoms/cm^2, converting to an erosion rate of 9.4×10^{15} C-atoms/(cm^2s) (about 1.0 nm/s).

Target element 5l TM1h3 showed no erosion at the strike line position but small deposition around 200 mm: This is consistent with the finding that the erosion on TDU 5l was generally lower than in most other TDUs, probably due to a slight misalignment of this TDU. Target element 5u TM1h3 showed a very similar erosion pattern as target elements TM2h6 with substantial erosion at the strike line. Target elements 5l TM3h6 and 5u TM3h6 also showed a very similar erosion pattern as target elements TM2h6 with smaller erosion in 5l and substantial erosion in 5u at the strike line with a maximum erosion of 1.1×10^{20} C-atoms/cm^2 (about 12 µm). This was also the highest measured erosion at the Standard strike line position of all marker tiles and converts to a maximum observed carbon erosion rate of 2.3×10^{16} C-atoms/(cm^2s) (about 2.5 nm/s).

Marker layers for erosion/deposition measurements were only available in target modules TM1h to TM3h. Some data about material deposition in target module TM4h can be found in [37].

The qualitative shape of the erosion pattern after OP 1.2b is comparable to the erosion pattern observed after OP 1.2a [9], except that the total erosion during OP 1.2b was smaller than during OP 1.2a. This will be discussed in more detail in section 3.4.

3.3.2 Vertical target modules

The erosion/deposition pattern on the vertical target elements TM1v5 and TM2v2, see Fig. 1, were qualitatively very similar to the pattern on the horizontal elements. TM2v2 in TDU 5l (Fig. 11) and 5u (Fig. 12) showed erosion at the strike line position around 150 mm and some carbon deposits towards the pumping gap at about 80 mm. Small erosion was observed close to the pumping gap and towards the inner wall. The erosion at the strike line of TDU 5l TM2v2, see Fig. 11, was higher than the initial carbon marker layer thickness, so that also the Mo interlayer was partly eroded. The most probable carbon erosion was extrapolated from the combined carbon and Mo erosion (dash-dotted line in Fig. 11) together with the uncertainty of this extrapolation (light grey are in Fig. 11). See section 3.2.1 for details. The erosion pattern on TDU 5u TM2v2 was considerably broader, but with a smaller maximum erosion, so that some fraction of the top carbon marker layer still was present and the underlying Mo interlayer has not been eroded.

Target elements TM1v5 in TDUs 5l and 5u showed no carbon erosion but thin deposits. Marker layers for erosion/deposition measurements were only available in target modules TM1v and TM2v. Some data about material deposition in target module TM3v can be found in [37].

3.4 Total carbon erosion

The toroidal distributions of carbon erosion integrated along the central line of target element TM2h6 is shown in Fig. 13 for both operational periods OP 1.2a [9] and OP 1.2b. Black bars indicate the directly measured C erosion, which is, however, often too low due to the complete erosion of the carbon marker at the strike line, see Figs. 10 and 11. The grey bars indicate the extrapolated carbon erosion based on the measured Mo erosion, see Figs. 10 and 11. The error bars take the uncertainty of this extrapolation (light grey areas in Figs. 10 and 11) into account. Note the different y-scales in Fig. 12 left and right. The carbon erosion on TDU 1l could not be determined during OP 1.2b due to the use of W-coated marker layers in this TDU [38].

The main difference between OP 1.2a and OP 1.2b is the considerably higher net erosion in OP 1.2a compared to OP 1.2b. The qualitative erosion pattern, however, is relatively similar in OP 1.2a and OP 1.2b: Both TDUs in module 2 showed the highest erosion, and TDU 5l had the lowest erosion in both operational periods. The difference of C erosion between the smallest erosion in 5l and the highest erosion in 2u is a factor of about two in both periods. Asymmetries in power fluxes were already observed by thermographic measurements [14] and are probably due to mechanical misalignments of TDUs with respect to the magnetic field. Qualitative similarities between OP 1.2a and OP 1.2b are therefore not astonishing, as the alignment of the TDUs was not changed between the two operational phases.

The observed erosion pattern is in rough agreement with the energy deposition with symmetrized trim coil currents to different TDU target modules determined by thermocouples (TCs) on the rear side of the target modules, see Fig. 12 in [39]. Higher temperature rises of the TCs were observed for TDUs 2u and 5u, lower temperature rises for TDUs 1l, 4u, 5l: This is in line with the observed net erosion pattern where higher erosion is observed in 2u and 5u and smaller erosion in 1l, 4u, 5l. The temperature rise was low in TDUs 3l and 3u: This is visible as low erosion in OP 1.2b, but not in OP 1.2a. These differences might be due to the fact that the net erosion is integrated over the whole campaign, while the TC temperature rise was only determined in individual discharges. The temperature rise of the TCs is proportional to the deposited energy, which in turn is approximately proportional to the gross carbon erosion. However, the net carbon erosion depends also on redeposition, which can be different in different TDUs due to locally different plasma parameters or impurity concentrations in the plasma.

When comparing OP 1.2a and OP 1.2b, it should be kept in mind that the discharge time in OP 1.2b was about 2.5 times longer than in OP 1.2a. A direct comparison of the total erosion therefore makes only limited sense, and it is more reasonable to compare the erosion rates. These are shown in Fig. 14. From OP 1.2a to OP 1.2b the net carbon erosion rate in standard configuration dropped by a factor of 5-6. The net carbon erosion rate in low iota configuration is lower as compared to the standard configuration by a factor of about 2. However, it should be kept in mind that the erosion at the strike line of the low iota configuration is a small net deposition area during standard configuration. The low erosion rate in low iota configuration therefore may be due to the fact that carbon eroded during low iota discharges is replaced by carbon deposited during standard discharges.

The erosion pattern varies from one target module to another in every TDU, and also varies between the different TDUs (see Fig. 13). According to the TC data from [39] on the horizontal target modules TM1h to TM5h (see Fig. 1) receive the highest power fluxes during standard configuration discharges. Power fluxes to TM6h and TM7h are already considerably smaller. For the determination of the total carbon erosion, we therefore only have to consider modules TM1h to TM5h in each of the 10 TDUs, i.e. in total 50 target modules in W7-X. Based on the thermographical images one can assume toroidal symmetry within each target module. Carbon erosion has been determined in poloidal direction on 13 horizontal target elements, which (assuming of toroidal symmetry within each target module) can be extrapolated to 13 horizontal target modules. For the remaining 37 horizontal target modules the erosion can be extrapolated based on the TC data from [39] with symmetrized trim coil currents assuming that the carbon erosion is proportional to the temperature rise of the TCs. For all 10 horizontal targets this results in 13.7±2.3 g of net carbon erosion, see Table 1.

For the vertical targets the situation is more difficult: Each vertical target consists of 3 target modules, i.e., in total 30 target modules in W7-X. Only at 4 of these the poloidal distribution of erosion has been measured, and TC data have not been published. We therefore have to assume identical erosion on the 10 vertical targets of the TDU. Based on thermography images we assume that 50% of the toroidal length of TM1v and 50% of the toroidal length of TM2v have full erosion and 50% of the toroidal length of TM2v have 50% erosion. With this assumption and the assumption of identical erosion in all TDUs, this gives a total carbon erosion at the vertical targets of 6.7±3.4 g. The total carbon erosion from the horizontal and vertical targets of all 10 TDUs was therefore 20.4±5.7 g carbon during OP 1.2b, see

Table 1. This has to be compared to the total carbon erosion of 48±5.7 g carbon during OP 1.2a, see Table 1. The net carbon erosion rate in OP 1.2a was 13.9±3.4 mg/s at the horizontal target and 4.2±1.8 mg/s at the vertical target in OP 1.2a, which dropped to 2.3±0.4 mg/s at the horizontal target and 0.9±0.5 mg/s at the vertical target in OP 1.2b.

4. Discussion

OP 1.2a was characterized by very high levels of C and O impurities in the plasma [10,11] due to outgassing of H_2O from graphite tiles [13]. Carbon was therefore eroded by physical and chemical erosion by oxygen ions, physical sputtering by carbon ions, and physical and chemical erosion by hydrogen. As already discussed in [9] the main erosion mechanism during OP 1.2a was chemical sputtering by oxygen due to formation of CO and (to a minor degree) CO_2 [40]. The ejected carbon atoms then could sputter further carbon atoms by physical sputtering. However, while self-sputtering of carbon can play an important role for maintaining the carbon concentration in the plasma, it plays a smaller role for net carbon erosion: Only sputtering yields above unity result in net erosion, while smaller sputtering yields still result in net deposition of carbon. The total erosion yield of carbon by hydrogen ions is only 0.01-0.03 C/H-ion at lower temperatures between room temperature and 600 K. At elevated temperatures around 800 K the chemical erosion yield by formation of CH_4 can reach values of 0.1 C/H-ion [41].

Boronizations in OP 1.2b resulted in a decrease of the oxygen and carbon concentrations in the plasma by 1-2 orders of magnitude [10, 11]. This decreased impurity concentration led to the described decrease of net carbon erosion at the TDU by a factor of 5-6. In OP 1.2b physical and chemical erosion of carbon by hydrogen and sputtering of carbon by carbon ions (and to a minor extend by other impurities like boron and oxygen) were probably the dominant erosion mechanisms. Sputtering by impurity ions is also the most probable erosion mechanism for explaining the observed erosion of the Mo layers at the strike line: Sputtering of Mo by hydrogen-ions is very low with a threshold energy of 201 eV [42].

5. Conclusions

The net erosion and deposition of carbon was determined at the test divertor unit (TDU) of W7-X during the operational phase OP 1.2b using 18 special PWI target elements. Target element TM2h6 was used in all TDUs, thus allowing to determine inhomogeneities between different TDUs. The target elements were coated with marker layers consisting of about 300 nm Mo and 5-10 μm C on top. The thicknesses of the marker layers were determined by elastic backscattering spectrometry (EBS) using 2.5 MeV protons before and after exposure.

Carbon erosion was observed at the strike line of the Standard configuration of all TDUs, a considerably smaller erosion was observed at the strike line of the Low Iota configuration. Some carbon deposition was observed left and right of the Standard configuration strike line. In total 20.4±5.7 g carbon were eroded from the TDU during OP 1.2b. The total net erosion on different TDUs scattered within a factor of

two between the TDU with the lowest and the highest erosion. The carbon erosion rate decreased by a factor of 5-6 compared to OP 1.2a due to boronizations: These decreased the oxygen concentrations considerably and resulted in a decrease of chemical erosion by formation of CO. The resulting decreased impurity concentrations enabled enhanced plasma operation.

More strongly eroded surfaces were considerably smoother compared to the initial material due to erosion/redeposition phenomena, which result in a higher erosion of hilltops and a filling of valleys with redeposited carbon. This smoothing effect results in a decrease of the arithmetic mean roughness and a decrease of the mean value of the microscopic inclination angle distribution, finally resulting in higher physical sputtering yields of plasma-exposed surfaces. This effect depends on particle fluence (or plasma exposure time): The plasma therefore creates its own surface structures which can be quite different from the initial surfaces. This renders investigations and numerical simulations of erosion/deposition phenomena even more difficult.

The maximum erosion rate in OP 1.2b at the strike line of the Standard configuration was 1-2.5 nm/s, depending on TDU and position in the TDU. Although this erosion rate is already a factor of 5-6 lower than in OP 1.2a, it is still challenging for long-pulse discharges with anticipated pulse lengths up to 1800 s. Long-pulse operation therefore may require a reduction of erosion by using either detached divertor conditions and/or a divertor material with lower erosion yield such as tungsten.

Acknowledgements

The technical assistance of J. Dorner and M. Fußeder from IPP Garching in all ion beam analysis measurements is gratefully acknowledged. Measurements using the optical profiler were made by K. Hunger.

This work has been carried out within the framework of the EUROfusion Consortium, funded by the European Union via the Euratom Research and Training Programme (Grant Agreement No 101052200 — EUROfusion). Views and opinions expressed are however those of the author(s) only and do not necessarily reflect those of the European Union or the European Commission. Neither the European Union nor the European Commission can be held responsible for them.

1 Beidler C *et al.* 1990 Physics and Engineering Design for Wendelstein VII-X *Fusion Technol.* **17** 148

2 Wolf R C *et al.* 2017 Major Results from the First Plasma Campaign of the Wendelstein 7-X Stellarator *Nucl. Fusion* **57** 102020

3 Bosch H-S *et al.* 2017 Final Integration, Commissioning and Start of the Wendelstein 7-X Stellarator Operation *Nucl. Fusion* **57** 116015

4 Sunn Pedersen T *et al.* 2017 Key Results from the First Plasma Operation Phase and Outlook for Future Performance in Wendelstein 7-X *Phys. Plasmas* **24** 055503

5 Peacock A *et al.* 2009 Progress in the Design and Development of a Test Divertor (TDU) for the Start of W7-X Operation *Fusion Eng. Des.* **84** 1475

6 Sunn Pedersen T *et al.* 2019 First Results from Divertor Operation in Wendelstein 7-X *Plasma Phys. Controlled Fusion* **61** 014035

7 Sunn Pedersen T, Otte M, Lazerson S, Helander P, Bozhenkov S, Biedermann C, Klinger T, Wolf R C, Bosch H -S and the Wendelstein 7-X Team 2016 Confirmation of the Topology of the Wendelstein 7-X Magnetic Field to Better than 1:100,000 *Nature Communications* **7** 13493

8 Hirsch M *et al.* 2008 Major Results from the Stellarator Wendelstein 7-AS *Plasma Phys. Controlled Fusion* **50** 053001

9 Mayer M *et al.* 2020 Material erosion and deposition on the divertor of W7-X *Phys. Scr.* **T171** 014035

10 Sereda S *et al.* 2020 Impact of boronizations on impurity sources and performance in Wendelstein 7-X *Nucl. Fusion* **60** 086007

11 Wang E *et al.* 2020 Impurity sources and fluxes in W7-X: from the plasma-facing components to the edge layer *Phys. Scr.* **T171** 014040

12 Fuchert G *et al* 2020 Increasing the density in Wendelstein 7-X: benefits and limitations *Nucl. Fusion* **60** 036020

13 Brezinsek S *et al.* 2022 Plasma-surface interaction in the Stellarator W7-X: conclusions drawn from operation with graphite plasma facing components *Nucl. Fusion* **62** 016006

14 Gao Y, Jakubowski M W, Drewelow P, Pisano F, Puig Sitjes A, Niemann H., Ali A, Cannas B and W7-X Team 2019 Methods for Quantitative Study of Divertor Heat Loads on W7-X *Nucl. Fusion* **59** 066007

15 Barbui T *et al.* 2018 The He/Ne beam diagnostic for active emission spectroscopy in the island divertor of Wendelstein 7-X, 45th EPS Conference on Plasma Physics, Prague, Czech Republic, P4.1018

16 Effenberg F *et al.* 2019 Investigation of 3D effects on heat fluxes in performance-optimized island divertor configurations at Wendelstein 7-X *Nucl. Mater. Energy* **18** 262

17 Dhard C P *et al.* 2021 Plasma-wall interaction studies in W7-X: main results from the recent divertor operations *Physica Scripta* **96** 124059

18 Dhard C P *et al.* 2017 Preparation of Erosion and Deposition Investigations on Plasma Facing Components in Wendelstein 7-X *Physica Scripta* **T170** 014010

19 Ruset C, Grigore E, Munteanu I, Maier H, Greuner H, Hopf C, Phylipps V and Matthews G 2009 Industrial Scale 10 µmW Coating of CFC Tiles for ITER-like Wall Project at JET *Fusion Eng. Des.* **84** 1662

20 Mayer M *et al.* 2020 Ion beam analysis of fusion plasma-facing materials and components: facilities and research challenges *Nucl. Fusion* **60** 025001

21 Dhard C P *et al.* 2019 Erosion and Deposition Investigations on Wendelstein 7-X First Wall Components for the First Operation Phase in Divertor Configuration *Fusion Eng. Des.* **146** 242

22 Mayer M 1997 SIMNRA User's Guide Technical Report IPP 9/113, Max-Planck-Institut für Plasmaphysik, Garching, Germany https://mam.home.ipp.mpg.de/Report%20IPP%209-113.pdf

23 Mayer M 2014 Improved Physics in SIMNRA 7 *Nucl. Instrum. Methods Phys. Res. B* **332** 176

24 Ziegler J F 2004 SRIM-2003 *Nucl. Instrum. Methods Phys. Res. B* **219–220** 1027

25 Gurbich A F 2016 SigmaCalc Recent Development and Present Status of the Evaluated Cross-Sections for IBA *Nucl. Instrum. Methods Phys. Res. B* **371** 27

26 Mayer M 2002 Ion Beam Analysis of Rough Thin Films *Nucl. Instrum. Methods Phys. Res. B* **194** 177

27 Guimarães R da S *et al.* 2021 Processing of massive Rutherford Back-scattering Spectrometry data by artificial neural networks *Nucl. Instrum. Methods Phys. Res. B* **493** 28

28 Cupak C *et al.* 2021 Sputter yields of rough surfaces: Importance of the mean surface inclination angle from nano- to microscopic rough regimes *Applied Surface Science* **570** 151204

29 Küstner M, Eckstein W, Dose V, and Roth J 1998 The influence of surface roughness on the angular dependence of the sputter yield *Nucl. Instrum. Methods Phys. Res. B* **145** 320

30 Küstner M, Eckstein W, Hechtl E and Roth J 1999 Angular dependence of the sputtering yield of rough beryllium surfaces *J. Nucl. Mater.* **265** 22

31 von Toussaint U, Mutzke A and Manhard A 2017 Sputtering of rough surfaces: a 3D simulation study *Physica Scripta* **T170** 014056

32 Arredondo R *et al.* 2019 Angle-dependent sputter yield measurements of keV D ions on W and Fe and comparison with SDTrimSP and SDTrimSP-3D *Nuclear Materials and Energy* **18** 72

33 Chodura R 1982 Numerical analysis of plasma-wall interaction for an oblique magnetic field *J. Nucl. Mater.* **111&112** 420

34 Zhao D, Yi R, Oelmann J, Brezinsek S, Rasinski M, Gao Y, Mayer M, Dhard C P, Krause M, W7-X team 2020 *Phys. Scr.* **T171** 014018

35 Zhao D *et al.* 2021 Quantification of erosion pattern using picosecond-LIBS on a vertical divertor target element exposed in W7-X *Nucl. Fusion* **61** 016025

36 Oelmann J *et al.* 2021 Hydrogen content in divertor baffle tiles in Wendelstein 7-X *Nuclear Materials and Energy* **26** 100943

37 Zhao M 2022 Distributions of deposits and hydrogen on the upper and lower divertor target elements of Wendelstein 7-X in preparation

38 Mayer M *et al.* 2021 Erosion of tungsten marker layers in W7-X *Phys. Scr.* **96** 124070

39 Lazerson S A *et al.* 2018 Error Fields in the Wendelstein 7-X Stellarator *Plasma Phys. Controlled Fusion* **60** 124002

40 Winter J 1996 Wall conditioning in fusion devices and its influence on plasma performance *Plasma Phys. Control. Fusion* **38** 1503

41 Balden M and Roth J 2000 New Weight-Loss Measurements of the Chemical Erosion Yields of Carbon Materials under Hydrogen Ion Bombardment *J. Nucl. Mater.* **280** 39

42 Eckstein W 2007 „Sputtering Yields“ in Behrisch R and Eckstein W (eds.) „Sputtering by Particle Bombardment”, Topics in Applied Physics 110 Springer Berlin Heidelberg ISBN 987-3-540-44500-5

Table 1: Total plasma time in operational phases OP1.2a and OP1.2b; carbon erosion on the horizontal and vertical TDU and the total (horizontal + vertical) carbon erosion on the TDU; carbon erosion rate on the horizontal and vertical TDU.

	OP1.2a	**OP1.2b**
Plasma time (s)	3775	9054
	Carbon erosion (g)	
Horizontal	34.5±8.4	13.7±2.3
Vertical	13.3±5.7	6.7±3.4
Total	47.8±14.1	20.4±5.7
	Carbon erosion rate (mg/s)	
Horizontal	13.9±3.4	2.3±0.4
Vertical	4.2±1.8	0.9±0.5

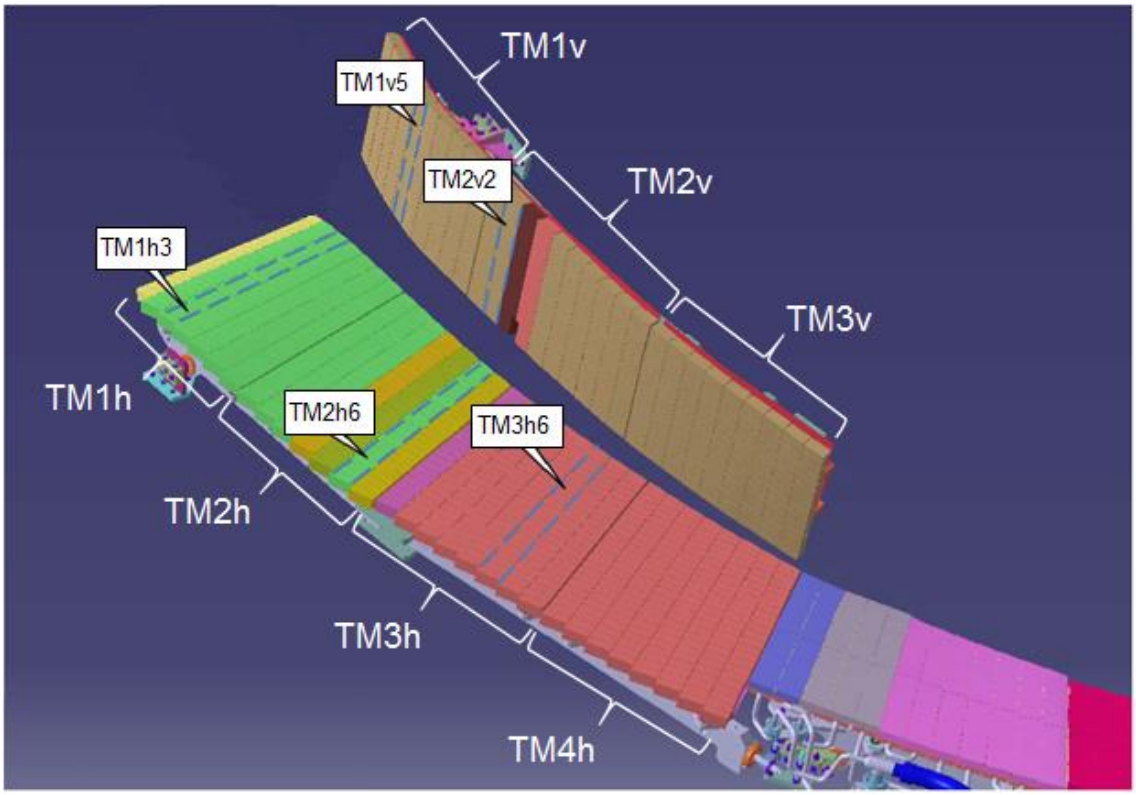

Figure 1: Schematic representation of the positions of the PWI target elements in the TDU. TM*x*h denotes horizontal target modules, TM*y*v are vertical target modules. TM*x*h*z* is the *z*'th element in target module *x*. From [9].

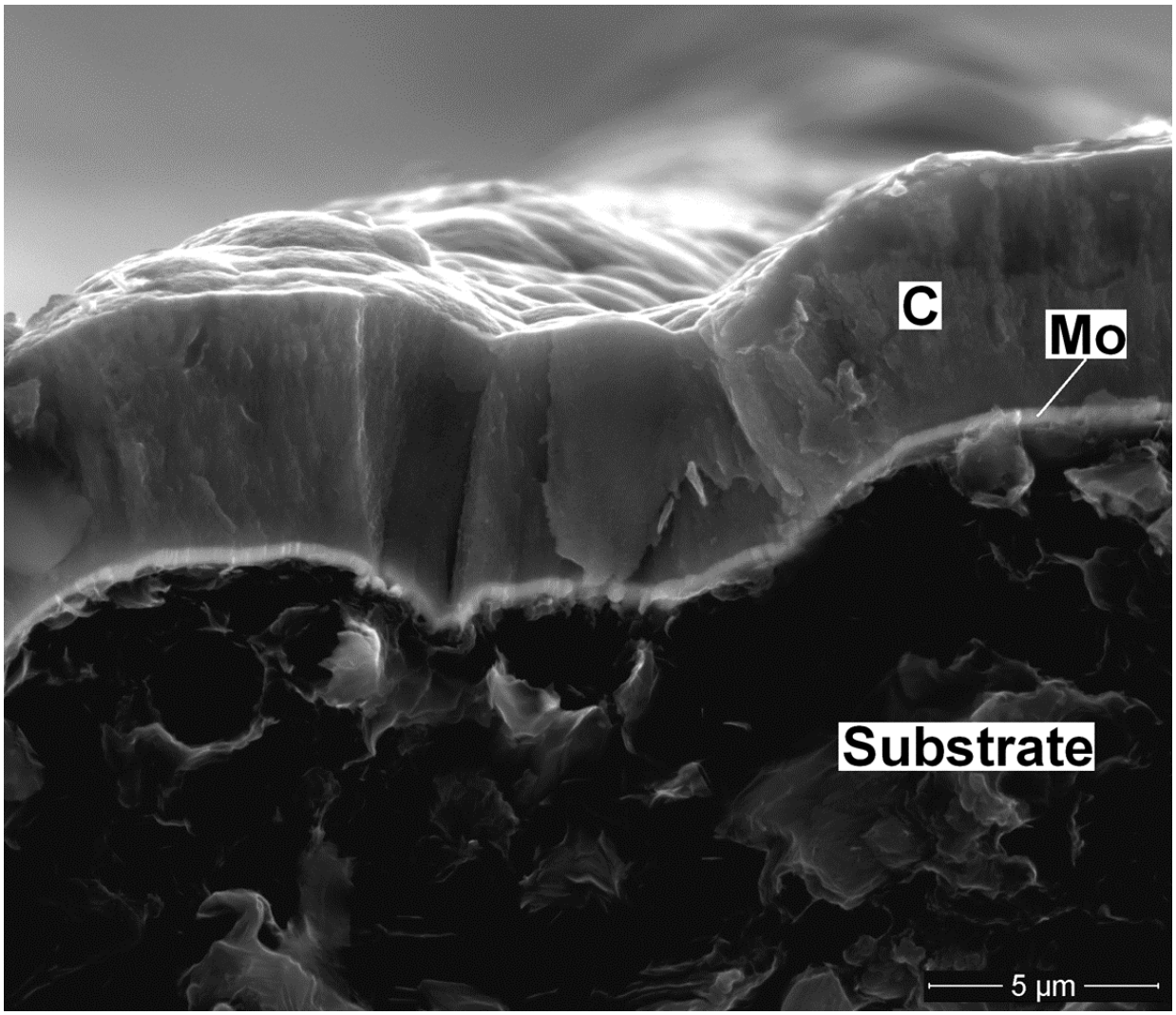

Figure 2: Scanning electron microscopy image of the fracture surface of the C/Mo marker coating before plasma exposure, showing the carbon marker coating (C), the Mo interlayer, and the fine-grain carbon substrate.

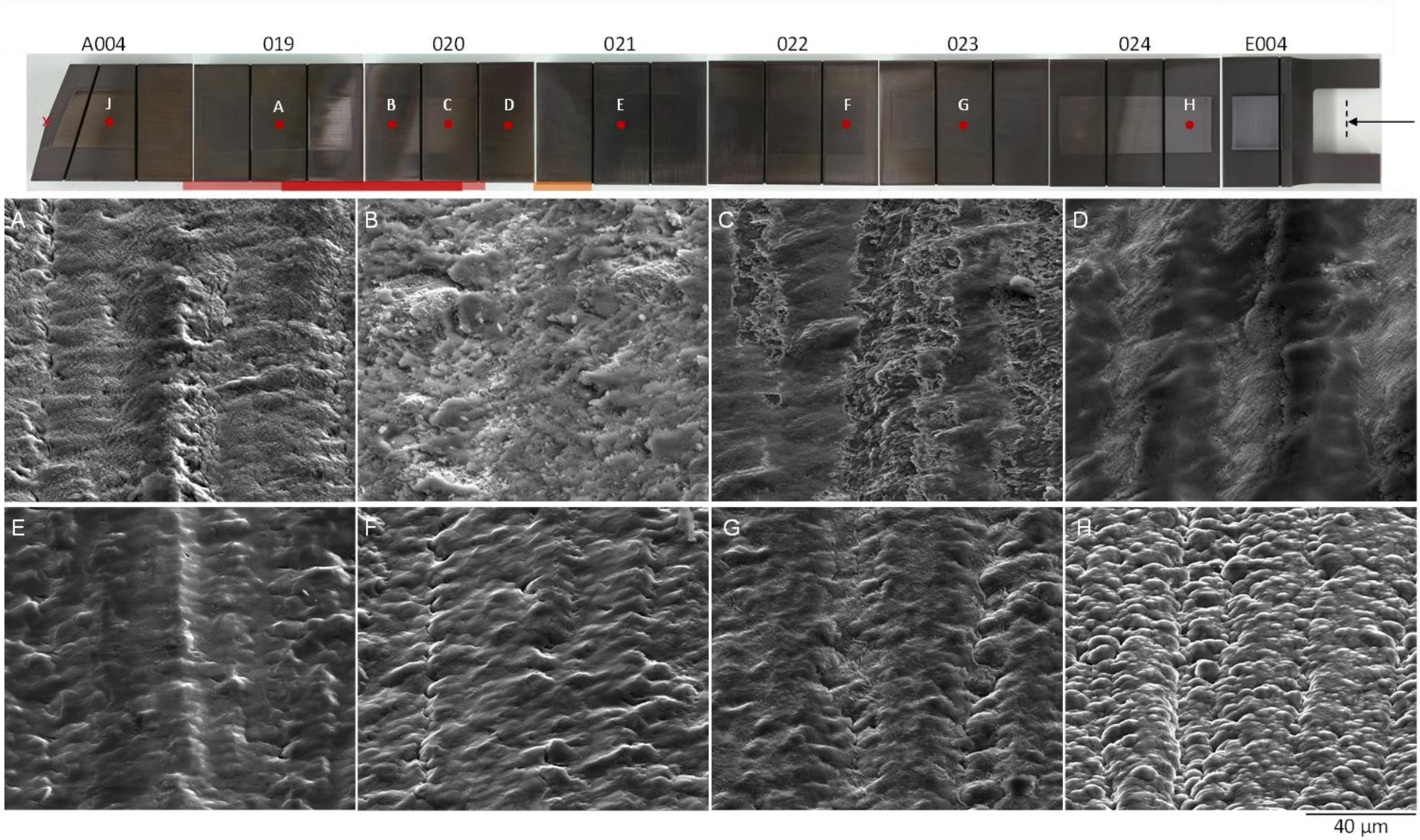

Figure 3: Top: Target element TM2h6 from TDU 2u after the operational period OP 1.2b. The target element consists of tiles A004, 019 to 024, and E004. The width of target elements 019 – 024 is 75 mm each. The red x at the left side of tile A004 marks the origin for the coordinate system used for IBA measurements. Red dots labeled A – H indicate positions where scanning electron micrographs are shown below and FIB cross-sections are shown in Fig. 4. The dashed line on the right hand side indicates the direction of the FIB cross-sections shown in Fig. 4, the arrow is the viewing direction. Roughness inclination angle distributions from positions C and J are shown in Figs. 6 and 7. The light red area below tiles 019 and 020 indicates the strike line area with net erosion, the dark red area

indicates the area with highest erosion. The orange area below tile 021 is an area with stronger net deposition. Bottom: Scanning electron micrographs from points A – H. Secondary electrons, tilt angle 52°.

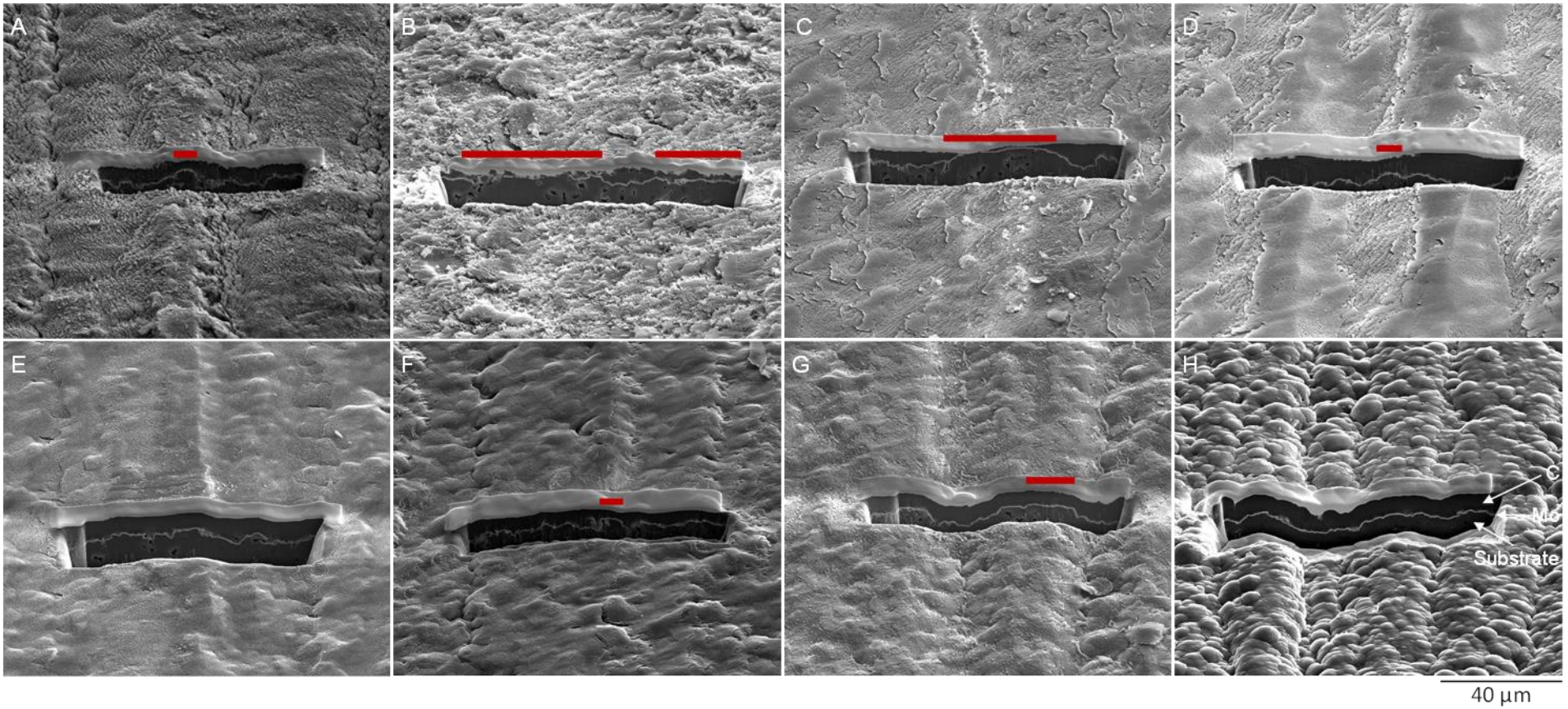

Figure 4: FIB cross-sections from positions A – H, see Fig. 3 for the positions and typical scanning electron micrographs of the surfaces. .The surface area of the cross-section has been coated with a thin Pt layer before cross-sectioning, this layer is visible behind the cross-section. The initial layer structure consisting of a 5–10 µm thick carbon layer on a thin Mo interlayer on the graphite substrate is labeled in subfigure H. Areas with potential erosion of the initial carbon marker layer are marked in red. Secondary electrons, tilt angle 52°.

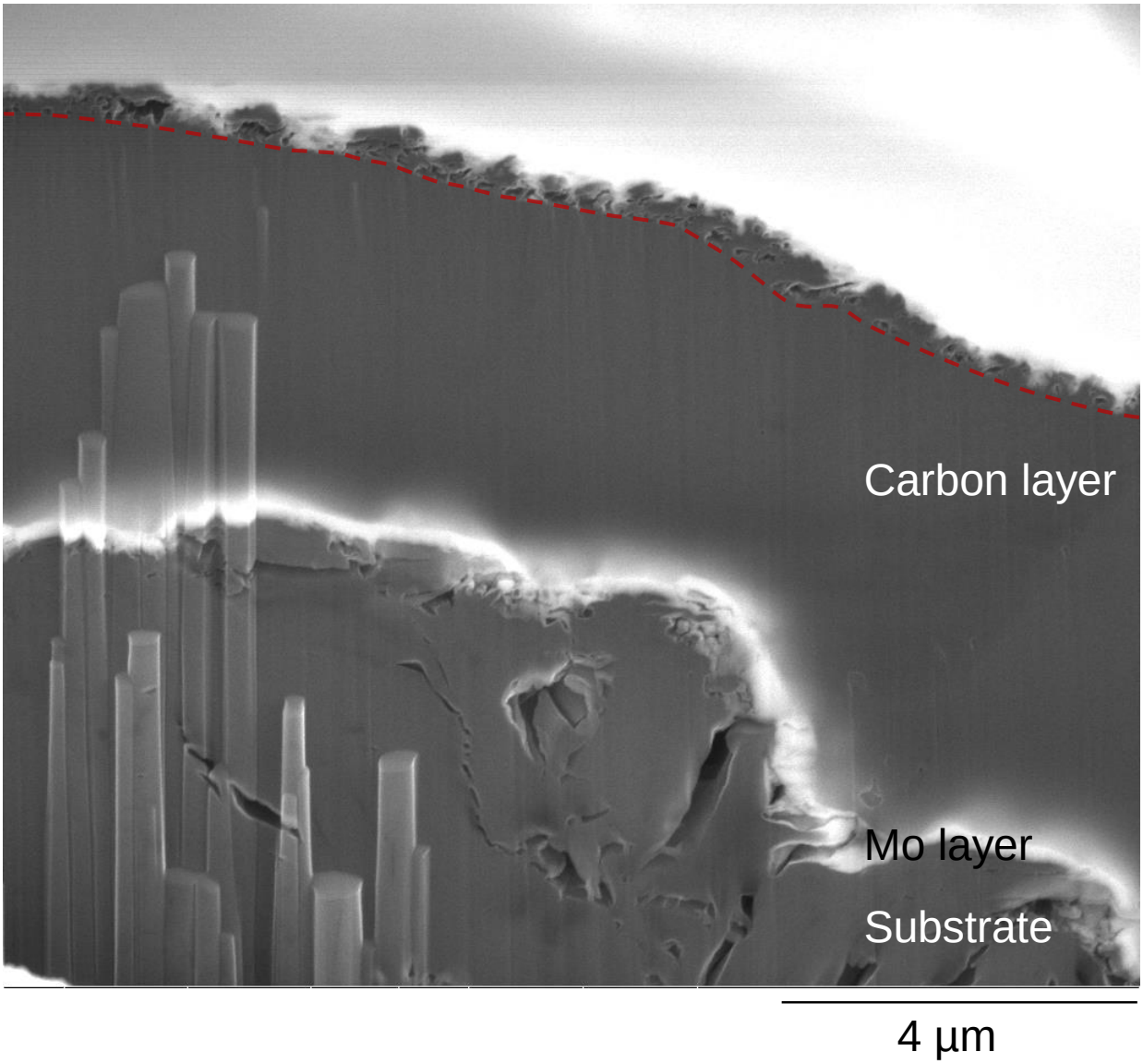

Figure 5: High resolution image of thin deposits at position G, see Fig. 3. The columnar structure in the lower left area of the cross-section is an artefact of the FIB cutting process. The initial surface is marked by the dashed red line. Secondary electrons, tilt angle 52°.

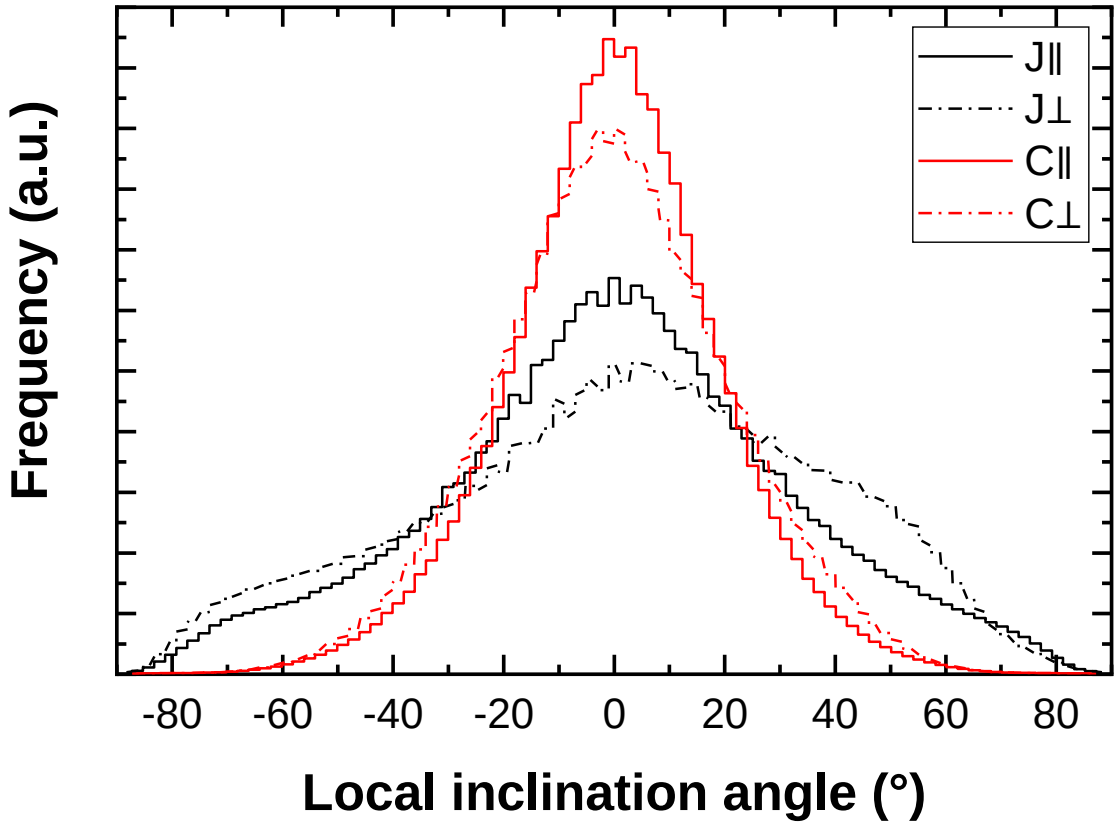

Figure 6: Frequency distribution of local inclination angles at positions J and C, see Fig. 3 top. ‖ is parallel to the grinding direction in poloidal direction, ⊥ is perpendicular to the grinding direction in toroidal direction. Bin width 2°.

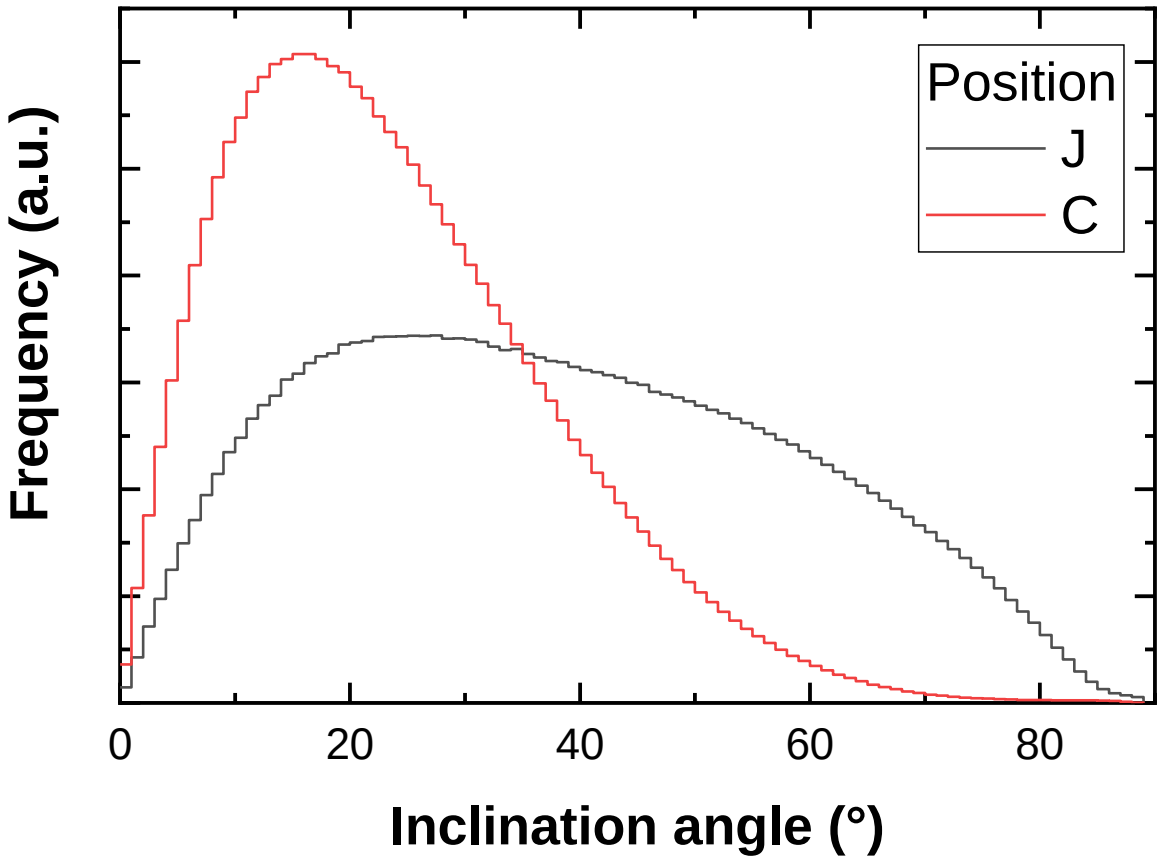

Figure 7: Frequency distribution of local planar inclination angles with respect to the nominal surface normal at positions J and C, see Fig. 3 top. Bin width 1°.

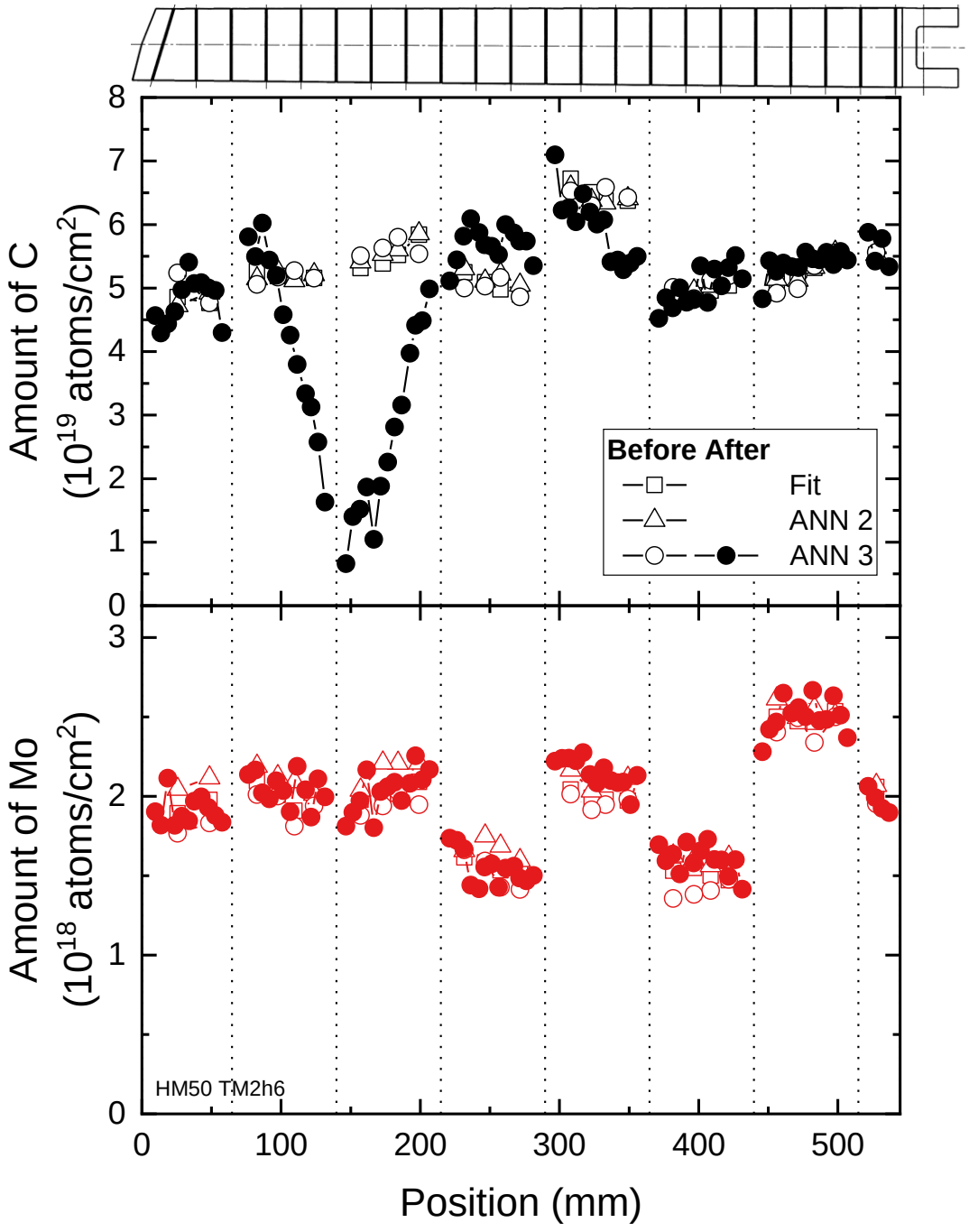

Figure 8: Thicknesses of the carbon (top) and molybdenum (bottom) marker layers before (hollow symbols) and after (solid symbols) exposure during OP 1.2b. Circles: thicknesses from the Artificial Neural Network analysis with 3 layers (ANN 3); Triangles: thicknesses from the Artificial Neural Network analysis with 2 layers (ANN 2); Squares: thicknesses from automatic fit. A schematic representation of the target

element is shown at the very top, dashed lines are tile boundaries. The pumping gap between the horizontal and the vertical targets, see figure 1, is on the left hand side. TDU 5l TM2h6.

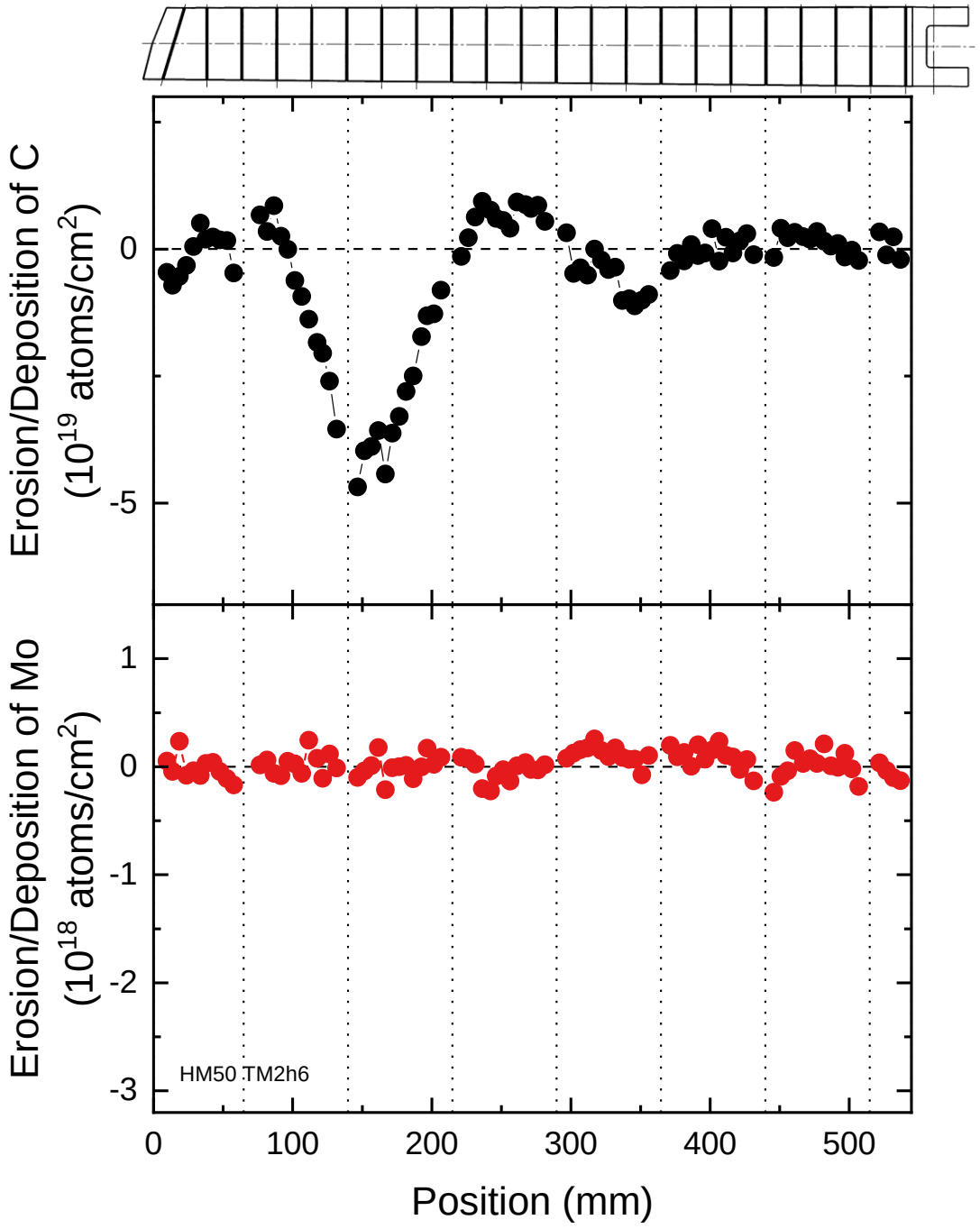

Figure 9: Net erosion of carbon (top) and molybdenum (bottom) from the marker layers during OP 1.2b based on the Artificial Neural Network analysis ANN 3. Deposition has positive, erosion negative sign. A schematic representation of the target element is shown at the very top, dashed lines are tile boundaries. The pumping gap between the horizontal and the vertical targets, see figure 1, is on the left hand side. TDU 5l TM2h6.

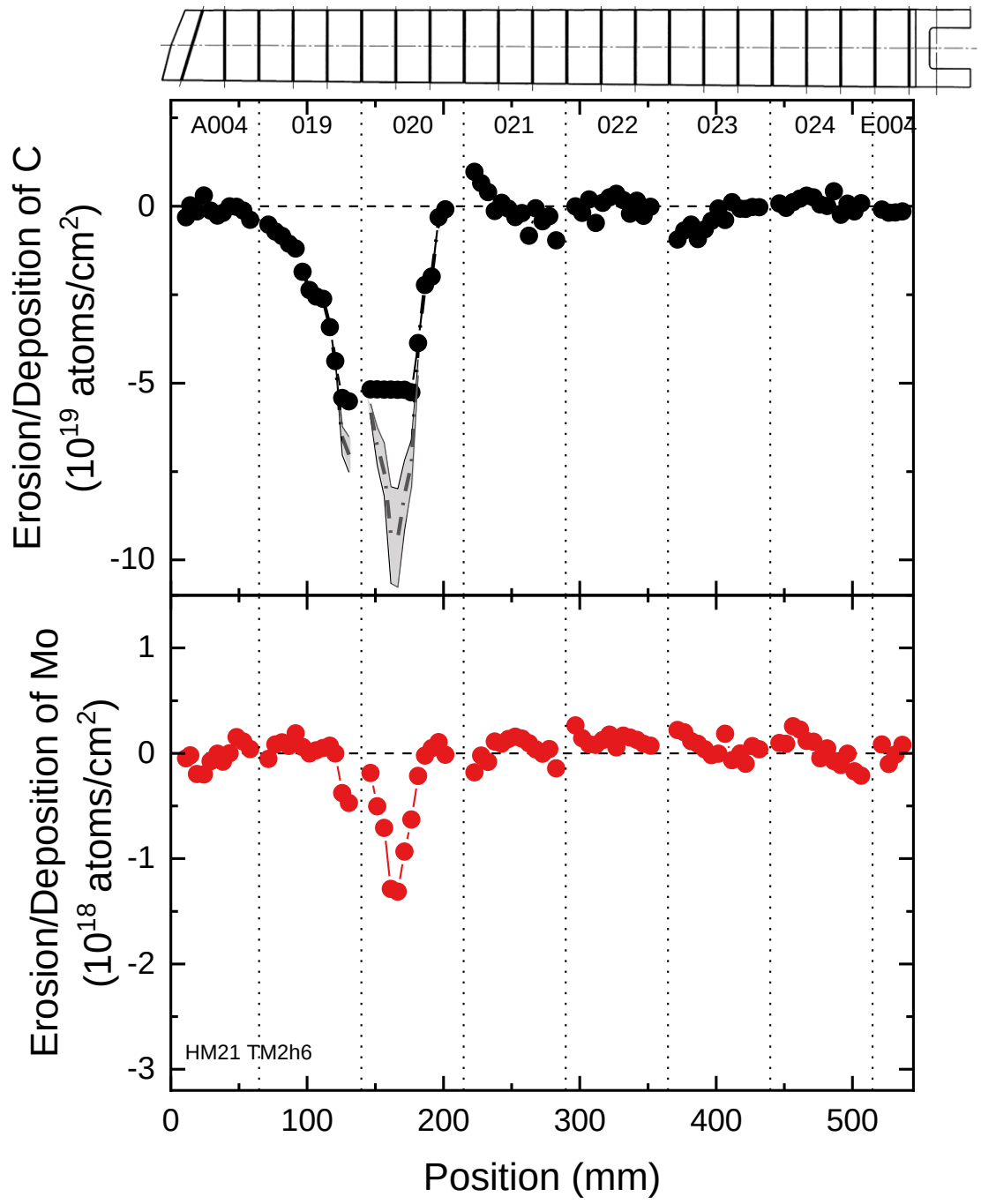

Figure 10: Net erosion of carbon (top) and molybdenum (bottom) from the marker layers during OP 1.2b based on the Artificial Neural Network analysis ANN 3. Deposition has positive, erosion negative sign. A schematic representation of the target element is shown at the very top, dashed lines are tile boundaries. The pumping gap between the horizontal and the vertical targets, see figure 1, is on the left hand side. TDU 2u TM2h6, see Fig. 3. Numbers at the top are tile numbers. Dash-dotted line: Extrapolated carbon erosion based on the erosion of the Mo layer; grey area: Uncertainty of the extrapolation.

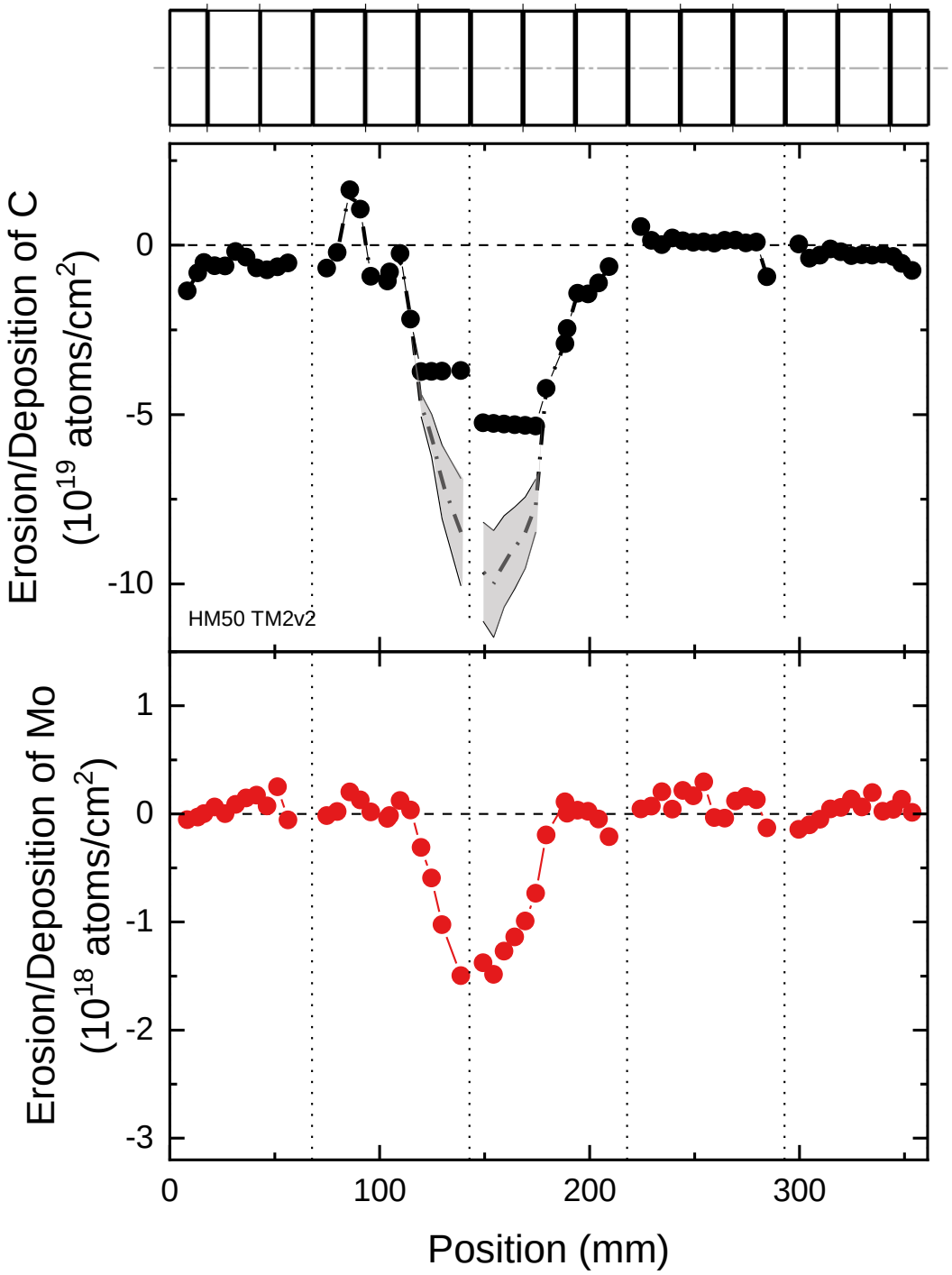

Figure 11: Net erosion of carbon (top) and molybdenum (bottom) from the marker layers during OP 1.2b based on the Artificial Neural Network analysis ANN 3. Deposition has positive, erosion negative sign. A schematic representation of the target element is shown at the very top, dashed lines are tile boundaries. The pumping gap between the horizontal and the vertical targets, see figure 1, is on the left hand side. TDU 5l TM2v2, see Fig. 3. Dash-dotted line: Extrapolated carbon erosion based on the erosion of the Mo layer; grey area: Uncertainty of the extrapolation.

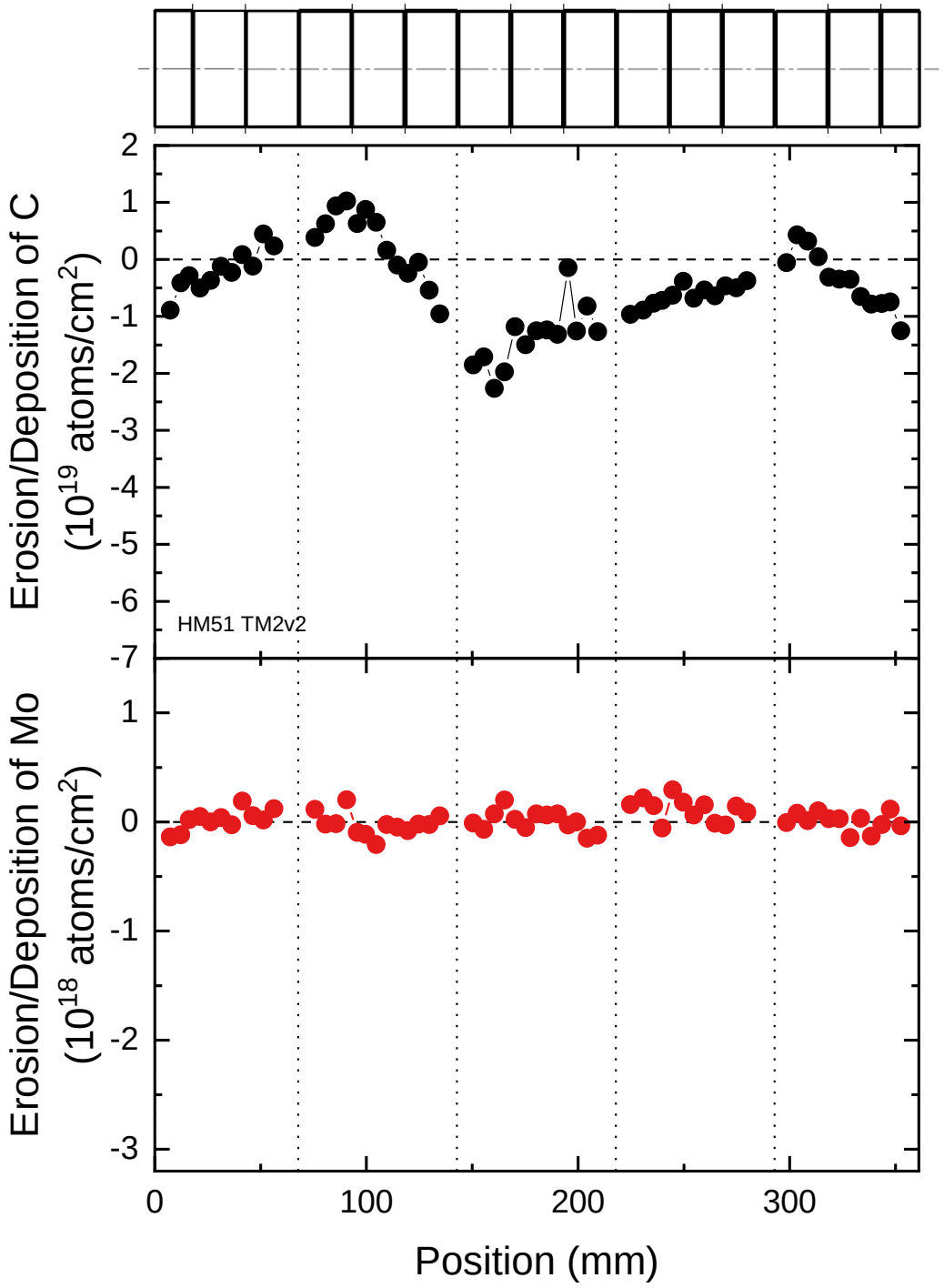

Figure 12: Net erosion of carbon (top) and molybdenum (bottom) from the marker layers during OP 1.2b based on the Artificial Neural Network analysis ANN 3. Deposition has positive, erosion negative sign. A schematic representation of the target element is shown at the very top, dashed lines are tile boundaries. The pumping gap between the horizontal and the vertical targets, see figure 1, is on the left hand side. TDU 5u TM2v2, see Fig. 3.

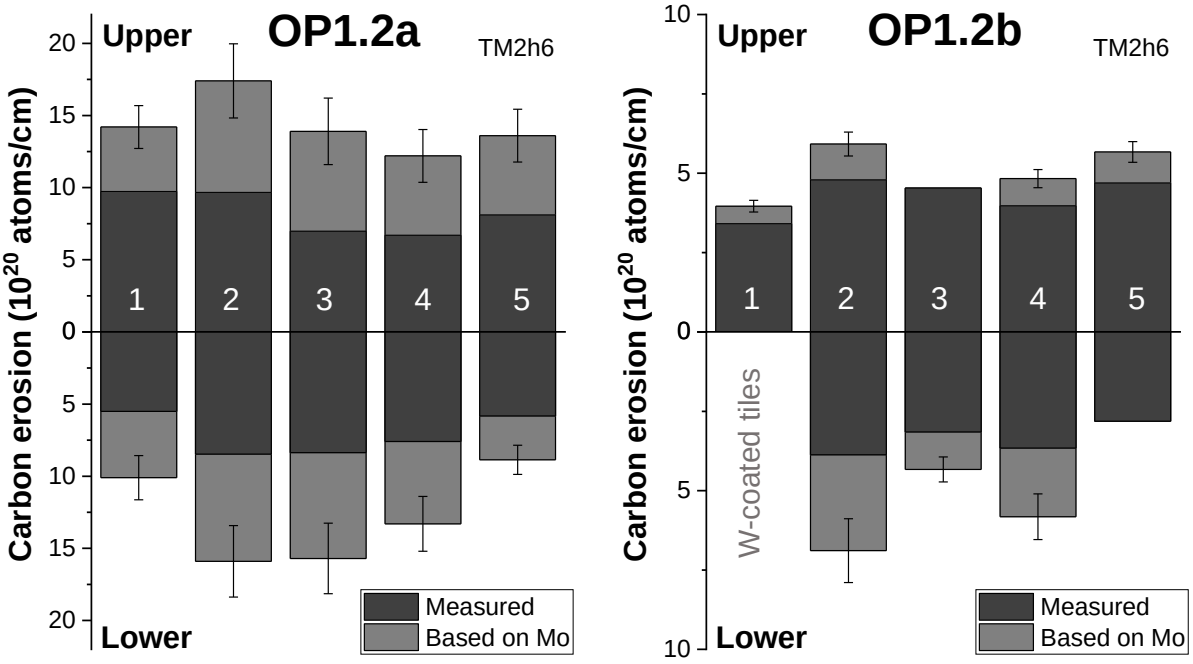

Figure 13: Erosion of carbon from the marker layers along the middle of target element TM2h6 in the upper and the lower TDUs in all 5 W7-X modules. Black bars: Measured carbon erosion; Grey bars: Carbon erosion extrapolated from the erosion of Mo, see figure 10. Uncertainties see figure 10. Left: Operational period OP1.2a; right: Operational period OP1.2b. Note the different y-scales of the left and right figures. During OP1.2b the carbon erosion on TDU 1l could not be determined due to the use of W-coated marker layers.

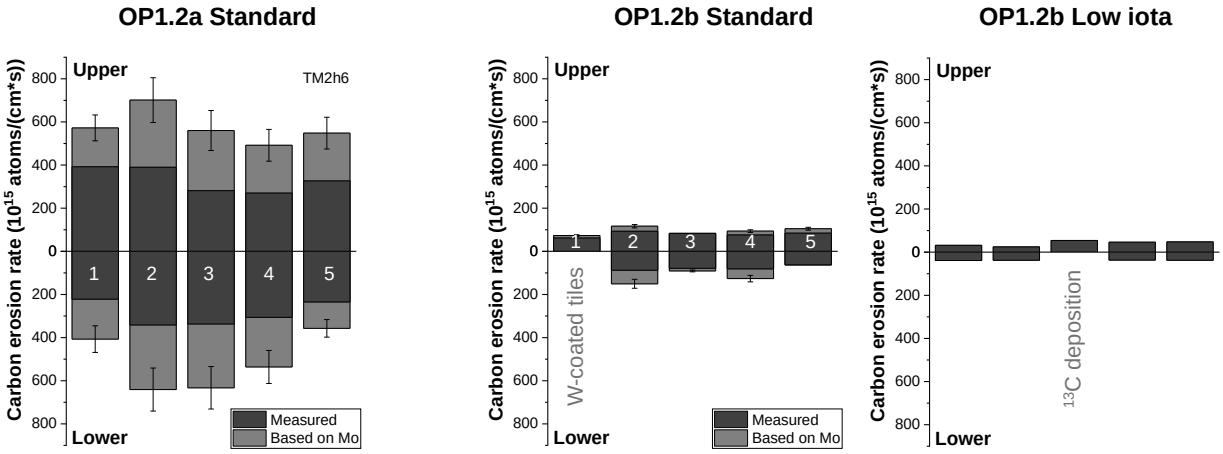

Figure 14: Carbon erosion rates from the marker layers along the middle of target element TM2h6 in the upper and the lower TDUs in all 5 W7-X modules. Black bars: Measured carbon erosion rates; Grey bars: Carbon erosion rates extrapolated from the erosion of Mo, see figure 10. Uncertainties see figure 10. Left: Operational period OP 1.2a standard configuration; middle: OP 1.2b standard configuration; right: OP 1.2b low iota configuration. During OP 1.2b the carbon erosion rate on TDU 1l could not be determined due to the use of W-coated marker layers. The carbon erosion rate on TDU 3l in low iota configuration could not be determined due to the formation of thick ^{13}C layers by puffing of $^{13}CH_4$ at this location.